Nanocrystal Catalysts

DOI: 10.1002/ange.201406497

Synthesis of Pt–Ni Alloy Nanocrystals with High-Index Facets and Enhanced Electrocatalytic Properties**

Xiling Xu, Xin Zhang, Hui Sun, Ying Yang, Xiaoping Dai, Jinsen Gao, Xueyong Li, Pengfang Zhang, Hong-Hui Wang, Neng-Fei Yu, and Shi-Gang Sun**

Abstract: *The shape-controlled synthesis of multicomponent metal nanocrystals (NCs) bounded by high-index facets (HIFs) is of significant importance in the design and synthesis of high-activity catalysts. We report herein the preparation of Pt–Ni alloy NCs by tuning their shape from concave-nanocubic (CNC) to nanocubic and hexoctahedral (HOH). Owing to the synergy of the HIFs and the electronic effect of the Pt–Ni alloy, the as-prepared CNC and HOH Pt–Ni alloy NCs exhibited excellent catalytic properties for the electrooxidation of methanol and formic acid, as well as for the oxygen reduction reaction (ORR).*

Owing to their high energy yield and low environmental pollution, polymer electrolyte fuel cells (PEFCs) are among the most promising energy-conversion technologies available today.[1] It has been well documented that among pure metals, Pt is the most efficient electrocatalyst for PEFCs. However, a number of obstacles associated with the use of Pt, including its insufficient activity, ready poisoning by intermediates generated in the reaction, and high cost, still hinder the commercial application of PEFCs.[2]

The shape-controlled synthesis of metal nanocrystals (NCs) has received extensive attention owing to its fascinating role in tuning the catalytic performance of the NCs. It has been recognized that the catalytic properties of platinum-containing nanostructures are strongly dependent on their morphology and composition,[3] and usually high-index facets (HIFs) of face-centered-cubic (fcc) metals with a high density of atomic steps, ledges, and kinks exhibit superior catalytic activity.[4] The alloying of different metal components is also a very effective way to improve the performance of nanocrystal catalysts because of electronic or synergistic effects.[4f,5] Consequently, the rational design and synthesis of well-defined alloy NCs is one of the focal points of frontier research.[5,6] Although the shape-controlled synthesis of monometallic NCs with HIFs has been studied extensively,[4e,7] alloy NCs bound by HIFs have been little explored to date[4f,5b,8] because of the difficulties in controlling high-energy surfaces in the presence of two metals with different nucleation and growth habits. Herein, we report a new synthetic strategy that enables the one-pot fabrication of concave-nanocubic (CNC) and hexoctahedral (HOH) Pt–Ni alloy NCs exclusively bound by HIFs by simply adjusting the concentration of glycine. To our great surprise, we found that CNC Pt–Ni alloy NCs were formed at a low concentration of glycine by self-assembly, which has never been observed previously in the synthesis of NCs with HIFs. However, HOH Pt–Ni alloy NCs could be evolved at a high concentration of glycine by crystal growth control.

The synthetic strategy is based on a one-pot wet-chemical reduction route involving polyvinylpyrrolidone (PVP), glycine, $NiCl_2$, and $H_2[PtCl_6]$ (Pt/Ni = 3:1, molar ratio). Pt–Ni alloy NCs of three different shapes, that is, concave nanocubes (CNCs), nanocubes, and hexoctahedra (HOHs), were obtained by simply adjusting the amount of glycine used (38, 58, and 88 mg, respectively). Glycine was shown to play the vital role in tuning the nucleation and growth rates of the Pt–Ni alloy NCs. These rates are well-established as the key factors in determining the morphology of NCs. To the best of our knowledge, CNC and HOH Pt–Ni alloy NCs exclusively bound by HIFs have not been synthesized previously. Specifically, the CNC and HOH Pt–Ni alloy NCs showed superior catalytic activity in the electrooxidation of methanol and formic acid, as well as the oxygen reduction reaction (ORR), in comparison with commercial platinum-black and Pt/C catalysts.

Figure 1a shows a representative scanning electron microscopy (SEM) image of as-prepared Pt–Ni alloy CNCs. The product shows a clear CNC structure, as demonstrated by high-resolution (HR) SEM, transmission electron microscopy (TEM), and high-angle annular dark-field scanning TEM (HAADF-STEM) (Figure 1b,c; see also Figure S1 in the Supporting Information). The products present excellent shape selectivity above 98% and an average apex-to-apex diameter of 53.4 nm (Figure 1c, inset). The angles between the facets of a representative Pt–Ni CNC projected along the [001] direction indicated by the selected-area electron diffraction (SAED) were determined to be approximately 10, 11, 14 and 16° (Figure 1d), which are in agreement with {610}, {510}, {410}, and {720}, respectively.[4g,5b,9] Nanoscale elemental mapping revealed that Pt and Ni were distributed

[*] X. Xu, Prof. Dr. X. Zhang, Dr. H. Sun, Dr. Y. Yang, Prof. Dr. X. Dai, Prof. Dr. J. Gao, X. Li, P. Zhang
State Key Laboratory of Heavy Oil Processing
College of Chemical Engineering, China University of Petroleum
Beijing 102249 (China)
E-mail: zhangxin@cup.edu.cn
H.-H. Wang, N.-F. Yu, Prof. Dr. S. G. Sun
State Key Laboratory for Physical Chemistry of Solid Surfaces
College of Chemistry and Chemical Engineering, Xiamen University
Xiamen 361005 (China)
E-mail: sgsun@xmu.edu.cn

[**] We thank the National Natural Science Foundation of China (No. 20903119, 21173269, 21321062, and 91127040) and the Ministry of Science and Technology of China (No. 2011BAK15B05).

Supporting information for this article is available on the WWW under http://dx.doi.org/10.1002/anie.201406497.

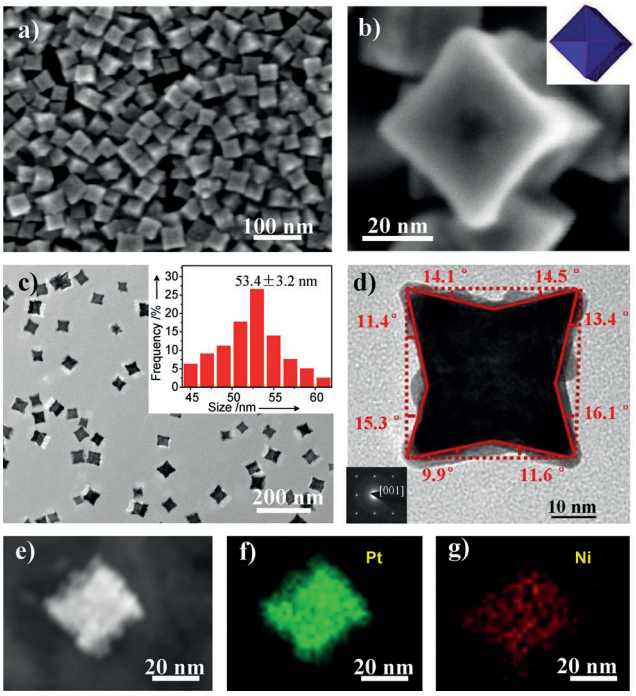

Figure 1. a) SEM, b) HRSEM (and corresponding model), c) TEM (and size-distribution histogram), and d) HRTEM images (and the corresponding SAED pattern) of CNC Pt–Ni alloy NCs. e) HAADF-STEM image and f, g) EDS-mapping images of the CNC Pt–Ni alloy NCs.

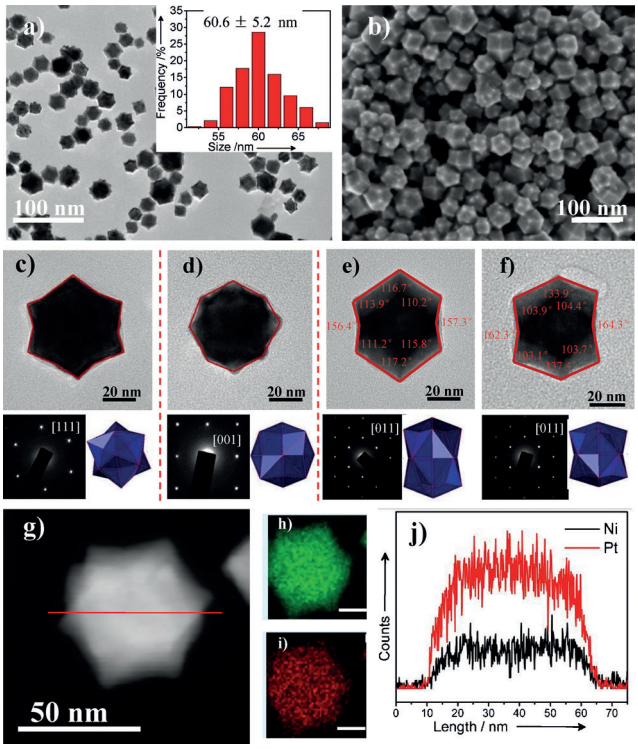

Figure 2. a) TEM (and size-distribution histogram) and b) SEM images of HOH Pt–Ni alloy NCs. c–f) TEM images and the corresponding SAED patterns and structural models of the HOH Pt–Ni alloy NCs viewed along the [111] (c), [001] (d), and [011] directions (e, f). g) HAADF-STEM image, h, i) EDS-mapping images (scale bars: 20 nm), and j) cross-sectional compositional line profiles of a HOH Pt–Ni NC.

uniformly throughout the entire CNC structure (Figure 1 e–g).

By increasing the glycine amount from 38 to 58 mg while keeping other synthetic conditions identical, we found that the products changed from CNCs to nanocubes. TEM and HAADF-STEM images revealed the formation of highly monodisperse and well-defined nanocubic Pt–Ni alloy NCs with an average edge length of 60.0 nm and a selectivity of about 70% for nanocubes (see Figure S2). The other morphologies are mainly CNC together with a minor amount of HOH Pt–Ni alloy NCs (see Figure S3). The as-prepared nanocubes were also well-alloyed, as verified by elemental mapping (see Figure S2).

Interestingly, concave HOH Pt–Ni alloy NCs were obtained when the amount of glycine used was further increased to 88 mg. Figure 2 a,b shows typical TEM and SEM images of the product and reveals the formation of high-purity (> 95%) HOH Pt–Ni alloy NCs with an average size of 60.6 nm. TEM images oriented along the [111], [001], [011] directions indicated by SAED and corresponding structural models further confirmed the formation of single-crystalline HOH Pt–Ni alloy NCs with HIFs (Figure 2 c–f).[4f,5a,7j] Figure 2 e,f shows typical TEM images of NCs viewed along the [011] zone axis. The measured projection angles formed between edge-on facets agree well with the calculated values for the {521} and {532} facets. Statistical analysis indicates that the majority of synthesized HOH Pt–Ni alloy NCs are enclosed by {521} facets (> 70%), and a minor proportion are bounded by {532} facets (< 30%; see Figure S4). The elemental mapping and compositional line-scanning profiles of Pt and Ni unambiguously verify that the distributions of Pt and Ni completely overlap (Figure 2 g–j).

It has been well established that the morphology of NCs depends on the nucleation and growth rates. The properties of reducing and stabilizing agents are important factors that influence the nucleation and growth rates of NCs. To investigate the formation mechanism of these Pt–Ni alloy NCs, we carried out a series of experiments. The reaction under the same conditions but without glycine in the solution afforded a large number of tiny spherical nanoparticles (3–5 nm in diameter) and cluster nanowires (see Figure S5 a). On the other hand, the reaction in the absence of PVP yielded only a few heavily aggregated nanoparticles (up to 5 μm) with irregular shapes (see Figure S5 b). Notably, at a growth time of 1 min, and with a glycine amount of 18, 38, and 58 mg under the other conditions unchanged, the Pt–Ni alloy NCs all had a spherical-like morphology with an average diameter of 2.7, 5.2, and 8.2 nm, respectively (see Figure S5 c–e). Although it is difficult to measure the specific composition of the initially formed small nanoparticles at this stage, we may infer that these small nanoparticles are Pt–Ni alloy NCs by characterization of the grown single particles (after the growth time of 6 h) on the basis of compositional line scanning and/or elemental mapping. When the growth time was increased to 6 h, the Pt–Ni alloy NCs evolved from a kind of special CNC to the CNC and then to the nanocube with an average size of

35.6, 53.4, and 60.0 nm, respectively (see Figure S6). These results demonstrate clearly that glycine plays a key role in the current shape-controlled synthesis. The presence of glycine can slow down the reduction rate of Pt^{IV} and Ni^{II} species through a strong coordination effect between metal ions and the amine or carboxy group of glycine,[6] as demonstrated by the reaction FTIR (see Figure S7) and UV/Vis spectra (see Figures S8 and S9), and therefore manipulate the nucleation and growth rates of the Pt–Ni alloy NCs. When the amount of glycine is increased under otherwise unchanged conditions, the nucleation rate becomes slower because of the slower reduction rate. However, once the crystal nucleus is formed, the growth rate of the Pt–Ni alloy NCs becomes faster owing to the higher concentration of Pt/Ni precursors that were less consumed in the nucleation stage. On the contrary, a much larger number of crystal nuclei is formed with a lower amount of glycine at a higher reduction and nucleation rate, and the growth rate of Pt–Ni alloy NCs becomes slower with the lower concentration of Pt/Ni precursors remaining. Although glycine can also function as the reducing agent, its reduction ability is much lower than that of PVP under the present reaction conditions.

PVP is essential for the formation of these Pt–Ni alloy nanostructures. The effect of the amount of PVP on the morphology of Pt–Ni alloy NCs with 38 mg of glycine was studied (see Figure S10). In the absence of PVP, the resulting products were heavily aggregated as mentioned above. The products formed when an amount of PVP of 100 mg was used had mixed morphologies, including CNC, cubic, and other polyhedral NCs. By further increasing the amount of PVP from 220 to 400 mg, the CNC morphology was retained; however, a change in the degree of concavity of the CNCs was clearly observed. On the basis of these results, PVP is thought to function as a reduction, dispersive, and stabilizing agent under the present conditions.

Zhang et al. earlier reported the glycine-mediated preparation of CNC Pt by a similar process.[4g] The well-defined CNC Pt was obtained with an appropriate amount (50–75 mg) of glycine in 1.5–12 h. Comparison of these two studies indicates that the addition of Ni^{2+} can significantly influence the morphology of Pt–Ni alloys. The presence of Ni can influence the reduction rate of Pt^{IV} species, as discussed below. In fact, the initial Pt/Ni molar ratio was identified as the key factor for the formation of well-defined CNC, nanocubic, and HOH Pt–Ni alloy NCs. For example, when the initial Pt/Ni molar ratio was changed from 3:1 to 1:1 and 1:3 under otherwise identical synthetic conditions of preparation of Pt–Ni CNCs, ill-defined Pt–Ni CNCs were obtained (see Figure S11).

A smaller amount of glycine results in a slower growth rate, which is helpful for investigation of the evolution process of Pt–Ni alloy NCs. We studied the course of the morphological evolution of Pt–Ni alloy NCs with 18 mg of glycine (Figure 3). The TEM image observed at 1 min shows tiny NCs with an average size of 2.7 nm (Figure 3a). At 20 min, Pt–Ni alloy NCs were slightly larger with an average size of 3.6 nm. Remarkably, a few aggregates were self-assembled by the small NCs. These aggregates appeared to be CNC, despite their ill-defined morphology (Figure 3b). Most of the small

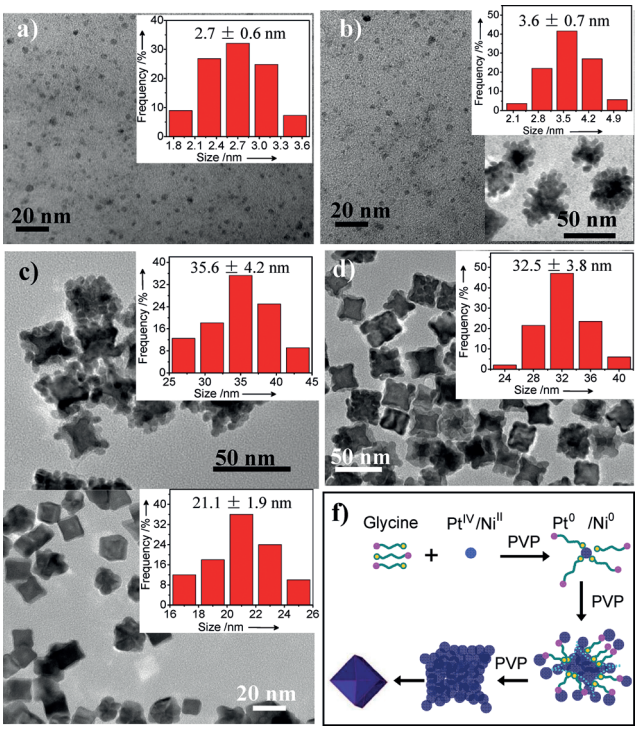

Figure 3. TEM images and size distribution (insert) demonstrating the course of the morphological evolution of Pt–Ni alloy NCs at a glycine amount of 18 mg. The reaction time was a) 1, b) 20 (the bottom-right inset shows a few aggregates), c) 360, d) 480, and e) 900 min. f) Illustration of the assembly process of Pt–Ni alloy CNCs.

Pt–Ni alloy NCs had disappeared after 360 min, and special Pt–NiCNCs with a high selectivity of 85 % and an average size of 35.6 nm had been produced. Notably, small spherical NCs were clearly observed in the shell of the special Pt–Ni CNCs (Figure 3c). The small spherical NCs could still be discerned in the shell at 540 min, whereas, interestingly, the average size of the special Pt–Ni alloy CNCs had decreased to 32.5 nm (Figure 3d). Well-defined Pt–Ni alloy CNCs with an average size of 21.1 nm were formed at 900 min (Figure 3e). The time-sequential evolution experiment clearly demonstrated that the Pt–Ni alloy CNCs were formed by a self-assembly process (Figure 3f). Assemblies of organic molecules, such as oleylamine and glycine, could act as soft templates to confine the growth of Pt–Ni alloy NCs through strong interactions between amine or carboxy groups and Ni^{II} or Pt^{IV} species.[10] Considering the abundance of carbonyl and hydroxy groups in the system, and because PVP is known to be a hydrogen-bond acceptor,[12] we presume that hydrogen bonding induced self-assembly to form of CNC Pt–Ni alloy NCs. The coordination of an amine, which also helps to stabilize the low-coordinated Pt–Ni sites, is the main reason why the HIFs can be preserved during the synthesis.[7e] Interestingly, the average size of Pt–Ni alloy NCs first increased from about 2.7 to 3.6 and 35.6 nm for reaction time of 1, 20 and 360 min, respectively, and then decreased to 32.5 and 21.1 nm when the reaction time was further increased to 540 and 900 min. The decrease in the average size can be ascribed to the formation of well-defined Pt–Ni alloy CNCs during the self-

assembly process, which removes the voids between small spherical Pt–Ni alloy NCs. Voids were clearly observed in the HAADF-STEM image (see Figure S12) of Pt–Ni alloy NCs at the early reaction time of 6 h. When the amount of glycine was increased to 38 mg, we still observed the self-assembly process for the formation of CNC Pt–Ni alloy NCs.

When the glycine amount was further increased, the growth rate of the Pt–Ni alloy NCs became very fast. We did not observe the self-assembly process for HOH Pt–Ni alloy NCs with a glycine amount of 88 mg. At a growth time of 1 min and with a glycine amount of 88 mg under the otherwise unchanged conditions, no particles were found. Small octahedral-like Pt–Ni alloy NCs were observed at 20 min. When the reaction time was increased to 30 min, the major particles were found to be HOH Pt–Ni alloy NCs together with a minor amount of nanocubes (see Figure S13). Well-defined HOH Pt–Ni alloy NCs were finally formed at 6 h. The results indicated that the shape evolution of the NC occurred from an octahedron enclosed by {111} to a nanocube enclosed by {100} facets, and then to a concave HOH enclosed by 48 {*hkl*} HIFs (see Figure S13 d),[4f,7h] thus demonstrating that the overgrowth of the Pt–Ni alloy NCs was more favorable at a slower reduction rate,[11] and the formation of HOH Pt–Ni alloy NCs was possible by the crystal growth control.[4f,7h]

UV/Vis spectra (see Figures S8 and S9) indicated that Pt^{IV} has a stronger coordination interaction with glycine than Ni^{II}, and the formation of dominated Pt^{IV} complex at the lower amount of glycine. Therefore, we deduce that glycine probably influences the reduction rates of Pt and Ni species. At a lower amount of glycine, Ni ions could first be reduced to Ni atoms, although the standard reduction potential of Ni^{2+}/Ni is more negative than that of Pt^{4+}/Pt, and then Pt^{IV} species could react with Ni by galvanic replacement. In other words, the presence of Ni could influence the reduction rate of Pt^{IV} species. At higher amounts of glycine, owing to formation of both Pt^{IV} and Ni^{II} complexes, the reduction rate of Pt^{IV} and Ni^{II} species could be different from that at a lower amount of glycine. On the basis of the above results, it can be concluded that glycine plays a key role by manipulating the reduction rate of Pt^{IV} and Ni^{II} species as well as the nucleation and growth rates of the Pt–Ni alloy NCs to form the CNC by self-assembly and the HOH by crystal-growth control.

The well-alloyed Pt–Ni alloy NCs were further confirmed by X-ray diffraction (XRD; Figure 4a). It was shown that the as-synthesized Pt–Ni alloy NCs possess a highly crystalline fcc Pt phase. The cell constant *a* of Pt–Ni alloy NCs was calculated to be approximately 3.87 Å, which is between those of pure Pt (3.92 Å) and Ni (3.52 Å). This result clearly demonstrates the formation of a Pt–Ni alloy, in which lattice contraction occurs as a result of the substitution of smaller nickel atoms for larger platinum atoms. The observation that the Pt–Ni alloy CNCs yield the highest {200} peak intensity, the HOHs feature the highest {220} peak intensity, and the nanocubes exhibit the enhanced {111} peak intensity indicates that these Pt–Ni alloy NCs have different preferential orientations. X-ray photoelectron spectra (XPS) show that these as-synthesized alloy NCs feature Pt $4f_{7/2}$ binding energies of 70.52–70.81 eV, thus demonstrating that the Pt species are metallic (Figure 4b). The negative shift of

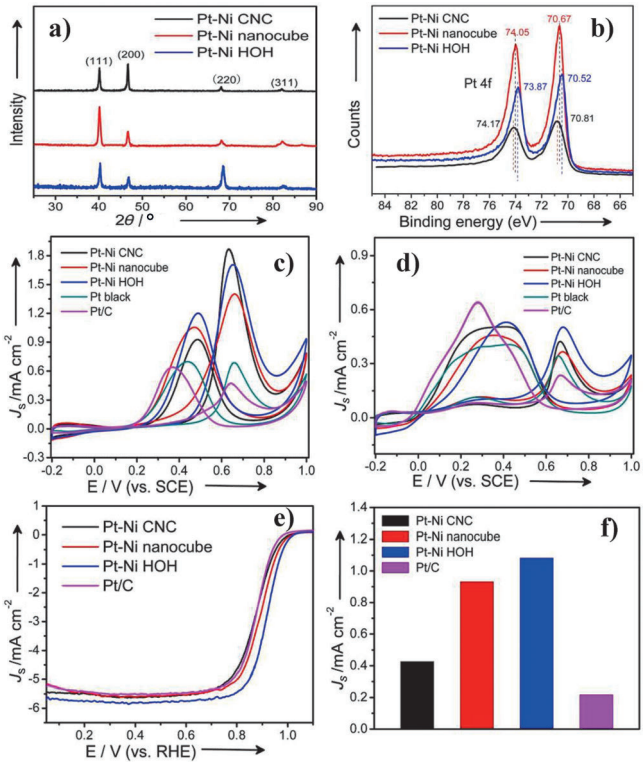

Figure 4. a) XRD spectra and b) XPS patterns of the Pt 4f of the as-prepared CNC, nanocubic, and HOH Pt–Ni alloy NCs. c) Cyclic voltammograms of the electrooxidation of methanol in a mixture of 0.5 M H_2SO_4 and 2 M CH_3OH at a scan rate of 50 mV s^{-1}. d) Cyclic voltammograms of the electrooxidation of formic acid in a mixture of 0.5 M H_2SO_4 and 0.25 M HCOOH at a scan rate of 50 mV s^{-1}. e) ORR polarization curves for the Pt–Ni HOHs, the Pt–Ni CNCs, the Pt–Ni nanocubes, and Pt/C, as recorded at room temperature in an O_2-saturated 0.1 M $HClO_4$ solution with a sweep rate of 10 mV s^{-1} and a rotation rate of 1600 rpm. f) Specific activity of the four catalysts at 0.90 V versus RHE.

approximately 0.09–0.38 eV as compared to pure metallic Pt ($4f_{7/2}$: 70.90 eV) is probably due to electron donation from Ni to Pt. In particular, the peak intensity of Ni 2p is quite weak (see Figure S14), and the surface compositions determined by XPS for Pt/Ni (molar ratio) are 94.6/5.4, 94.2/5.8, and 94.0/6.0, which are much higher than the values of 83.6/16.4, 82.4/17.6, and 80.0/20.0 determined by inductively coupled plasma optical emission spectrometry (ICP-OES) for the CNC, nanocubic, and HOH Pt–Ni alloy NCs, respectively (see Table S1 in the Supporting Information). This result indicates that Pt is enriched on the surface of Pt–Ni alloy NCs.

The electrooxidation of methanol and formic acid and the oxygen reduction reaction (ORR) were used to probe the effects of shape on the electrocatalytic properties of the as-prepared Pt–Ni alloy NCs. For comparison, commercial Pt black and Pt/C catalysts were measured as reference materials under the same conditions. Before each electrochemical test, Pt–Ni alloy NCs were washed extensively with a mixture of deionized water and ethanol, and then treated by UV–ozone (UVO) cleaning, as described for the earlier study,[3c,4g] to further remove the capping agents.[5b,6b] The morphology of

the Pt–Ni alloy NCs after removal of the capping agents remained intact, as demonstrated by FTIR spectroscopy (see Figure S15) and TEM characterization (see Figure S16) of the CNC Pt–Ni alloy NCs.

Figure 4c,d compares the cyclic voltammograms (CVs) for the electrooxidation of methanol and formic acid, respectively, on the CNC, nanocubic, and HOH Pt–Ni alloy NCs, and commercial Pt black and Pt/C catalysts. The electrochemically active surface area (ECSA) was measured by hydrogen adsorption/desorption and the underpotential deposition of Cu (UPD-Cu method; see Figure S17 and Table S2).[13] We considered the synthesized Pt–Ni alloys as electrochemical catalysts without a carbon support or hydrogen spillover effect, and that charge density in the UPD-Cu method is structure-dependent,[13] which may present uncertainties for CNC, nanocubic, and HOH Pt–Ni alloy NCs with their different morphologies and facets. The specific current density (J_s) was normalized to the ECSA measured by the hydrogen-adsorption/desorption method (see Figure S18). The peak current densities for methanol (and formic acid) oxidation in the positive potential scan were measured at 1.71 (0.51), 1.86 (0.45), 1.40 (0.37), 0.68 (0.34), and 0.47 (0.23) mA cm^{-2} on the Pt–Ni HOHs, Pt–Ni CNCs, Pt–Ni nanocubes, commercial Pt black, and commercial Pt/C, respectively. It is evident that the electrocatalytic activity of the Pt–Ni nanocubes is superior to that of Pt/C and Pt black, thus demonstrating that the binary alloy structure significantly improves the electrochemical performance of the catalyst. Interestingly, the electrocatalytic activity of the HOH and CNC Pt–Ni alloy NCs with exposed {*hkl*} and {*hk*0} HIFs was much higher than that of the Pt–Ni nanocubes or Pt/C and Pt black catalysts. The oxidation current density on HOH and CNC Pt–Ni alloy NCs was almost 2.5 (1.5) and 2.7 (1.3) times that observed for Pt black, and 3.6 (2.2) and 3.9 (1.9) times that of Pt/C in the electrooxidation of methanol (formic acid), respectively. The HOH and CNC Pt–Ni alloy NCs also demonstrated good stability in the electrooxidation of both methanol and formic acid, as indicated by J_s–t curves for 1000 s and structure characterization thereafter (see Figure S19). More importantly, further electrochemical measurement of the ORR indicated that the specific activities (at 0.90 V versus RHE) of the HOH (1.08 mA cm^{-2}), nanocubic (0.93 mA cm^{-2}), and CNC Pt–Ni alloy NCs (0.44 mA cm^{-2}) are 5, 4, and 2 times, respectively, as high as that of Pt/C (0.22 mA cm^{-2}), as based on the ECSA (Figure 4e,f), thus demonstrating the highly enhanced activities of Pt–Ni alloy NCs, which were recently reported as efficient catalysts for the ORR.[14]

These above results demonstrated that HOH and CNC Pt–Ni alloy NCs with HIFs consisting of high-density atomic steps and kinks exhibit enhanced catalytic activity per unit surface area for the oxidation of small organic molecules, such as methanol and formic acid, as well as the ORR, as compared to that of commercial Pt black and Pt/C catalysts. The excellent properties of the HOH and CNC Pt–Ni alloy NCs could be attributed to the synergy of the HIFs and the electronic effect of the Pt–Ni alloy. However, in terms of catalytic activity per unit weight of Pt, the overall activity of these larger HOH and CNC Pt–Ni alloy NCs is approximately 80% that of 3 nm commercial Pt nanoparticles (see Figure S20). It is evident that Pt–Ni alloy NCs of smaller sizes are important for applications, and such NCs can also be prepared by the present synthetic strategy. For example, the use of 8.9 mg of glycine afforded CNC Pt–Ni alloy NCs with an average apex-to-apex diameter of 9.5 nm (see Figure S21). Future improvement of the synthetic process is in progress to produce smaller Pt–Ni alloy NCs with HIFs.

In summary, CNC and HOH Pt–Ni alloy NCs with HIFs were synthesized by a simple wet-chemical method for the first time. The experimental results revealed that the CNC and HOH Pt–Ni alloy NCs exhibit much higher specific activity and stability for the electrooxidation of methanol and formic acid, as well as for the ORR, than those of the Pt–Ni nanocubes and commercial Pt/C and Pt black catalysts. Glycine played a key role by manipulating the nucleation and growth rates of Pt–Ni alloy NCs to form the CNC by self-assembly and the HOH by crystal-growth control. The synthetic strategy involving the self-assembly of bimetallic alloy NCs with HIFs is expected to have potential application in the preparation of other binary (e.g., Pt–Co alloy NCs, as shown in Figure S22) and even ternary metallic alloy nanostructures.

Experimental Section

Preparation of Pt–Ni alloy NCs: PVP (MW = 30000, 220 mg), glycine (8.9 mg for the Pt–Ni CNCs with an average size of 9.5 nm, 18 mg for the special CNCs, 38 mg for the CNCs, 58 mg for nanocubes, 88 mg for the HOHs), aqueous $NiCl_2$ solution (1.66 mM, 4 mL), and aqueous $H_2[PtCl_6]$ solution (20 mM, 1 mL) were mixed and stirred for 5 min, and then sonicated in an ultrasonic bath for 5 min at room temperature. The resulting homogeneous yellow solution was transferred to a 20 mL Teflon-lined stainless-steel autoclave. The sealed vessel was heated at 200°C for 6 h before it was cooled to room temperature. The products were separated by centrifugation at 9200 rpm for 15 min and further purified by washing with ethanol three times.

Details of nanocrystal characterization, the electrooxidation of methanol and formic acid, and the ORR are given in the Supporting Information.

Received: June 23, 2014
Published online: September 2, 2014

Keywords: alloys · electrocatalysis · electrooxidation · oxygen reduction reaction · nanocrystals

[1] a) A. S. Aricò, S. Srinivasan, V. Antonucci, *Fuel Cells* **2001**, *1*, 133–161; b) V. D. Colle, V. Grozovski, E. Herrero, J. M. Feliu, *ChemCatChem* **2013**, *5*, 1350–1354.

[2] a) Y. Yu, H. L. Xin, R. Hovden, D. Wang, E. D. Rus, J. A. Mundy, D. A. Muller, H. D. Abruña, *Nano Lett.* **2012**, *12*, 4417–4423; b) M. C. Orilall, F. Matsumoto, Q. Zhou, H. Sai, H. D. Abruña, F. J. DiSalvo, U. Wiesner, *J. Am. Chem. Soc.* **2009**, *131*, 9389–9393; c) F. J. Vidal-Iglesias, J. Solla-Gullón, E. Herrero, A. Aldaz, J. M. Feliu, *J. Appl. Electrochem.* **2006**, *36*, 1207–1212.

[3] a) Y. Kang, C. B. Murray, *J. Am. Chem. Soc.* **2010**, *132*, 7568–7572; b) D. S. Wang, Y. D. Li, *Prog. Chem.* **2013**, *25*, 1–7; c) Z. C. Zhang, J. F. Hui, Z. G. Guo, Q. Y. Yu, B. Xu, X. Zhang, Z. C. Liu, C. M. Xu, J. S. Gao, X. Wang, *Nanoscale* **2012**, *4*, 2633–2639.

[4] a) M. K. Carpenter, T. E. Moylan, R. S. Kukreja, M. H. Atwan, M. M. Tessema, *J. Am. Chem. Soc.* **2012**, *134*, 8535–8542; b) F.

Wang, C. Li, L. D. Sun, H. Wu, T. Ming, J. Wang, J. C. Yu, C. H. Yan, *J. Am. Chem. Soc.* **2011**, *133*, 1106 – 1111; c) J. Wu, J. Zhang, Z. Peng, S. Yang, F. T. Wagner, H. Yang, *J. Am. Chem. Soc.* **2010**, *132*, 4984 – 4988; d) A. X. Yin, X. Q. Min, Y. W. Zhang, C. H. Yan, *J. Am. Chem. Soc.* **2011**, *133*, 3816 – 3819; e) Y. Yu, Q. Zhang, B. Liu, J. Y. Lee, *J. Am. Chem. Soc.* **2010**, *132*, 18258 – 18265; f) L. Zhang, J. Zhang, Q. Kuang, S. Xie, Z. Jiang, Z. Xie, L. Zheng, *J. Am. Chem. Soc.* **2011**, *133*, 17114 – 17117; g) Z. C. Zhang, J. F. Hui, Z. C. Liu, X. Zhang, J. Zhuang, X. Wang, *Langmuir* **2012**, *28*, 14845 – 14848; h) Y. G. Sun, Y. N. Xia, *Science* **2002**, *298*, 2176 – 2179; i) N. Tian, Z. Y. Zhou, S. G. Sun, *J. Phys. Chem. C* **2008**, *112*, 19801 – 19817.

[5] a) Z. Quan, Y. Wang, J. Fang, *Acc. Chem. Res.* **2013**, *46*, 191 – 203; b) A. X. Yin, X. Q. Min, W. Zhu, W. C. Liu, Y. W. Zhang, C. H. Yan, *Chem. Eur. J.* **2012**, *18*, 777 – 782.

[6] a) Y. J. Deng, N. Tian, Z. Y. Zhou, R. Huang, Z. L. Liu, J. Xiao, S. G. Sun, *Chem. Sci.* **2012**, *3*, 1157 – 1161; b) Z. Zhang, Y. Yang, F. Nosheen, P. Wang, J. Zhang, J. Zhuang, X. Wang, *Small* **2013**, *9*, 3063 – 3069.

[7] a) N. Tian, Z. Y. Zhou, S. G. Sun, Y. Ding, Z. L. Wang, *Science* **2007**, *316*, 732 – 735; b) X. Kou, W. Ni, C. K. Tsung, K. Chan, H. Q. Lin, G. D. Stucky, J. Wang, *Small* **2007**, *3*, 2103 – 2113; c) T. Ming, W. Feng, Q. Tang, F. Wang, L. D. Sun, J. F. Wang, C. H. Yan, *J. Am. Chem. Soc.* **2009**, *131*, 16350 – 16354; d) N. Tian, Z. Y. Zhou, N. F. Yu, L. Y. Wang, S. G. Sun, *J. Am. Chem. Soc.* **2010**, *132*, 7580 – 7584; e) X. Huang, Z. Zhao, J. Fan, Y. Tan, N. Zheng, *J. Am. Chem. Soc.* **2011**, *133*, 4718 – 4721; f) M. Jin, H. Zhang, Z. Xie, Y. Xia, *Angew. Chem. Int. Ed.* **2011**, *50*, 7850 – 7854; *Angew. Chem.* **2011**, *123*, 7996 – 8000; g) X. Xia, J. Zeng, B. McDearmon, Y. Zheng, Q. Li, Y. Xia, *Angew. Chem. Int. Ed.* **2011**, *50*, 12542 – 12546; *Angew. Chem.* **2011**, *123*, 12750 – 12754; h) T. T. Tran, X. M. Lu, *J. Phys. Chem. C* **2011**, *115*, 3638 – 3645; i) Y. Y. Li, Y. X. Jiang, M. H. Chen, H. G. Liao, R. Huang, Z. Y. Zhou, N. Tian, S. P. Chen, S. G. Sun, *Chem. Commun.* **2012**, *48*, 9531 – 9534; j) J. W. Hong, S. U. Lee, Y. W. Lee, S. W. Han, *J. Am. Chem. Soc.* **2012**, *134*, 4565 – 4568; k) J. Xiao, S. Liu, N. Tian, Z. Y. Zhou, H. X. Liu, B. B. Xu, S. G. Sun, *J. Am. Chem. Soc.* **2013**, *135*, 18754 – 18757.

[8] a) Y. Yu, Q. Zhang, X. Lu, J. Y. Lee, *J. Phys. Chem. C* **2010**, *114*, 11119 – 11126; b) H. Zhang, M. Jin, J. Wang, M. J. Kim, D. Yang, Y. Xia, *J. Am. Chem. Soc.* **2011**, *133*, 10422 – 10425; c) L. Zhang, W. Niu, Z. Li, G. Xu, *Chem. Commun.* **2011**, *47*, 10353; d) C. L. Lu, K. S. Prasad, H. L. Wu, J. A. Ho, M. H. Huang, *J. Am. Chem. Soc.* **2010**, *132*, 14546 – 14549.

[9] a) T. Yu, D. Y. Kim, H. Zhang, Y. Xia, *Angew. Chem. Int. Ed.* **2011**, *50*, 2773 – 2777; *Angew. Chem.* **2011**, *123*, 2825 – 2829; b) J. Zhang, M. R. Langille, M. L. Personick, K. Zhang, S. Li, C. A. Mirkin, *J. Am. Chem. Soc.* **2010**, *132*, 14012 – 14014.

[10] a) Z. Huo, O. K. Tsung, W. Huang, X. Zhang, P. Yang, *Nano Lett.* **2008**, *8*, 2041 – 2046; b) H. You, S. Yang, B. Ding, H. Yang, *Chem. Soc. Rev.* **2013**, *42*, 2880 – 2904.

[11] B. Lim, X. Lu, M. Jiang, P. H. C. Camargo, E. C. Cho, E. P. Lee, Y. Xia, *Nano Lett.* **2008**, *8*, 4043 – 4047.

[12] a) S. A. Jenekhe, X. L. Chen, *Science* **1998**, *279*, 1903 – 1907; b) L. Wang, S. Cui, Z. Wang, X. Zhang, *Langmuir* **2000**, *16*, 10490 – 10494.

[13] a) S. Trasatti, O. A. Petrii, *Pure Appl. Chem.* **1991**, *63*, 711 – 734; b) M. Shao, J. H. Odeii, S.-I. Chai, Y. Xia, *Electrochem. Commun.* **2013**, *31*, 46 – 48.

[14] a) V. R. Stamenkovic, B. Fowler, B. S. Mun, G. Wang, P. N. Ross, C. A. Lucas, N. M. Markovic, *Science* **2007**, *315*, 493 – 497; b) S. Choi, S. Xie, M. Shao, J. H. Odell, N. Lu, H. C. Peng, L. Protsailo, S. Guerrero, J. Park, X. Xia, J. Wang, M. J. Kim, Y. Xia, *Nano Lett.* **2013**, *13*, 3420 – 3425; c) C. Chen, Y. J. Kang, Z. Y. Huo, Z. W. Zhu, W. Y. Huang, H. L. L. Xin, J. D. Snyder, D. G. Li, J. A. Herron, M. Mavrikakis, M. F. Chi, K. L. More, Y. D. Li, N. M. Markovic, G. A. Somorjai, P. D. Yang, *Science* **2014**, *343*, 1339 – 1343.

